Draft version January 27, 2021
Typeset using LaTeX twocolumn style in AASTeX62

Radial Gradients in Dust Opacity Lead to Preferred Region for Giant Planet Formation

Yayaati Chachan,[1] Eve J. Lee,[2,3] and Heather A. Knutson[1]

[1]Division of Geological and Planetary Sciences, California Institute of Technology, 1200 E California Blvd, Pasadena, CA, 91125, USA
[2]Department of Physics and McGill Space Institute, McGill University, 3550 rue University, Montréal, QC, H3A 2T8, Canada
[3]Institute for Research on Exoplanets, Montréal, QC, Canada

ABSTRACT

The Rosseland mean opacity of dust in protoplanetary disks is often calculated assuming the interstellar medium (ISM) size distribution and a constant dust-to-gas ratio. However, the dust size distribution and the dust-to-gas ratio in protoplanetary disks are distinct from those of the ISM. Here, we use simple dust evolution models that incorporate grain growth and transport to calculate the time evolution of mean opacity of dust grains as a function of distance from the star. Dust dynamics and size distribution are sensitive to the assumed value of the turbulence strength α_t and the velocity at which grains fragment $v_{\rm frag}$. For moderate-to-low turbulence strengths of $\alpha_t \lesssim 10^{-3}$ and substantial differences in $v_{\rm frag}$ for icy and ice-free grains, we find a spatially non-uniform dust-to-gas ratio and grain size distribution that deviate significantly from the ISM values, in agreement with previous studies. The effect of non-uniform dust-to-gas ratio on the Rosseland mean opacity dominates over that of the size distribution. Spatially varying—that is non-monotonic—dust opacity creates a region in the protoplanetary disk that is optimal for producing hydrogen-rich planets, potentially explaining the apparent peak in gas giant planet occurrence rate at intermediate distances. Enhanced opacities within the ice line also suppress gas accretion rates onto sub-Neptune cores, thus stifling their tendency to undergo runaway gas accretion within disk lifetimes. Finally, our work corroborates the idea that low mass cores with large primordial gaseous envelopes ('super-puffs') originate beyond the ice line.

1. INTRODUCTION

Dust opacity plays an important role in setting the temperatures and vertical structures of protoplanetary disks (e.g., Chiang & Goldreich 1997; D'Alessio et al. 1998) and determines how rapidly a planet accretes its gaseous envelope (e.g., Stevenson 1982; Pollack et al. 1996; Ikoma et al. 2000). The temperature structure of the disk determines where various molecules can condense, resulting in a spatially and temporally varying division of elements between solid and gas phases (e.g. Hayashi 1981; Oberg et al. 2011). In the core accretion framework, dust opacity regulates the cooling of the envelope accreted by a growing planet (e.g., Piso & Youdin 2014; Lee et al. 2014; Piso et al. 2015). Because the envelope accretion rate is cooling-limited during the hydrostatic phase of planetary growth, this dust opacity also has a strong influence on the final envelope mass.

In particular, cooling-limited accretion determines which planetary cores reach the threshold for runaway gas accretion within the gas disk lifetime and hence influences the giant planet occurrence rate. Radial velocity surveys indicate that giant planets inside 7 au only occur around 10% of FGK stars and they predominantly orbit their host stars at intermediate distances ($3-5$ au); their occurrence rate declines at both smaller and larger orbital distances (Cumming et al. 2008; Howard et al. 2012; Wittenmyer et al. 2016; Fernandes et al. 2019; Fulton et al. 2019; Wittenmyer et al. 2020; complemented by direct imaging surveys, e.g. Bowler & Nielsen 2018; Baron et al. 2019). It is unclear why giant planets preferably occur at intermediate distances. The water ice line is typically assumed to play a role in making this region favorable for giant planet formation, primarily by facilitating the formation of massive cores (e.g. Morbidelli et al. 2015). However, the role of gas accretion in shaping the occurrence rate of giant planets remains largely unexplored.

Sub-Neptunes dominate the observed population of exoplanets with orbital periods less than 300 days (e.g., Batalha et al. 2013; Fressin et al. 2013; Morton & Swift 2014; Dressing & Charbonneau 2015; Petigura et al. 2018). The measured radii and masses of sub-Neptunes are consistent with hydrogen and helium envelope mass fractions of a few percent (Wolfgang & Lopez 2015; Ning et al. 2018), despite the fact that some of these planets have cores massive enough ($\gtrsim 10 M_\oplus$) to reach the threshold for runaway gas accretion. What regulates the envelope mass fraction at a few percent? It has been suggested that the accretion of material with

Corresponding author: Yayaati Chachan
ychachan@caltech.edu

high dust opacity could prevent these planets from amassing significantly larger envelopes (e.g. Lee et al. 2014; Chen et al. 2020). Here, we revisit this idea and explore why sub-Neptunes might be expected to form close-in whereas gas giants are more common at larger orbital separations.

Determining the dust opacity at a given location in the protoplanetary disk is a non-trivial task as it depends on the poorly known optical properties (composition and structure), size distribution, and dust-to-gas ratio, all three of which are intricately coupled to the protoplanetary disk's structure and evolution. Previous studies in both the protoplanetary disk and planet formation literature (e.g. Bell & Lin 1994; Alexander & Ferguson 1994a) have generally elected to adopt a single global value for the dust-to-gas ratio and a power-law size distribution (both the power-law index and the bounding grain sizes) that is akin to that of dust in the interstellar medium (ISM). However, such a prescription is too simplistic to calculate the mean opacity due to dust grains in a protoplanetary disk. Dust grains in protoplanetary disks grow to sizes that are significantly larger (mm-cm size, e.g. Miyake & Nakagawa 1993; Testi et al. 2003; Draine 2006; Andrews 2015) than the largest sub-micron sized grains in the ISM (Draine & Lee 1984). The maximum grain size has a profound influence on both the short-wavelength and mean opacities of protoplanetary disks as the mass distribution of grains is top heavy (e.g. D'Alessio et al. 2001).

Fortunately, advances in our understanding of grain coagulation and the role of fragmentation and radial drift in limiting grain growth now make it possible to calculate the grain size distribution as a function of location in protoplanetary disks (Brauer et al. 2008; Birnstiel et al. 2010, 2011). In a recent study, Savvidou et al. (2020) assessed the effect of varying grain size distribution from coagulation and fragmentation on the Rosseland mean opacity and the thermal structure of the disk, but without taking dust transport into account. Transport of dust due to radial drift, gas drag, and turbulent diffusion leads to a radially-varying dust-to-gas ratio, which may significantly alter dust opacity.

In this work, we use a published dust evolution model to calculate the spatial and temporal evolution of the dust-to-gas ratio in a protoplanetary disk (Birnstiel et al. 2012) in § 2. We then calculate the corresponding Rosseland mean opacity using an approximate size distribution scheme to determine the grain size distribution as a function of distance from the star (Birnstiel et al. 2015). In § 3, we compute the disk opacity dust evolution models as a function of radial distance, height from midplane, and time and show that our results differ starkly from the usual ISM opacity values. We then use our updated opacity values to calculate gas accretion rates onto planetary cores and discuss the consequences of our work for the formation of gas giants, sub-Neptunes, and 'super-puffs' (low mass planets with sizes beyond $\sim 4\,R_\oplus$) in § 4. We summarize our results and suggest potential directions for future work in § 5.

2. MODELS

2.1. *ISM size distribution*

The ISM size distribution is usually described using a power law distribution:

$$n(a) = A\, a^{\beta}, \tag{1}$$

where n is the number of particles per unit volume per unit size interval, A is a normalization factor that depends on the assumed dust-to-gas ratio and the minimum and maximum grain sizes, and β is the power law index that characterises how bottom- or top-heavy the size distribution is. The power law index β and minimum and maximum grain sizes (a_{min} and $a_{\max}$) are typically chosen to be −3.5, 0.005μm, and 0.25μm, respectively, which fit the observed extinction law in the diffuse interstellar medium (Mathis et al. 1977; Laor & Draine 1993; Alexander & Ferguson 1994b). Although there are small variations in the values used for these parameters in the published literature, especially a_{min} and $a_{\max}$, they do not make an appreciable difference for the calculated opacity. The value for the normalizing constant A is given by:

$$A = \frac{3\rho_d(\beta+4)}{4\pi\rho_s(a_{\max}^{\beta+4} - a_{min}^{\beta+4})}, \tag{2}$$

where ρ_s = 1.675 g cm^{-3} is the material density of the dust grain, fixed to a value appropriate for the DSHARP mixture (see § 2.3), ρ_d is the density of dust in the disk, ρ_g the density of disk gas, and $\epsilon = \rho_d/\rho_g$ is the dust-to-gas ratio. The ISM dust opacity is typically calculated assuming a global value of $\epsilon = 0.01$ for the entire protoplanetary disk. For ρ_g, we use the gas density in the disk midplane obtained from our protoplanetary disk model, which we describe in the next section.

2.2. *Protoplanetary disk model*

We use the publicly available code `twopoppy` to model the structure of a protoplanetary disk and the dynamics of dust and gas[1]. The methods and algorithms used in `twopoppy` are described in Birnstiel et al. (2012) and we will present a brief overview here for completeness. We consider a protoplanetary disk of mass 0.1 M_* around a protostar of mass $M_* = 0.7\,M_\odot$. The stellar effective temperature (T_*) and radius (R_*) are set to 4010 K and 1.806 $R_\odot$ respectively.

[1] The original public repository is available at https://github.com/birnstiel/two-pop-py. A fork of this repository with the changes implemented in our work is available at https://github.com/y-chachan/two-pop-py.

We assume that the disk is passively heated, and its temperature structure therefore takes the following form (e.g. Chiang & Goldreich 1997; D'Alessio et al. 1998):

$$T(r) = \left[\phi\, T_*^4 \left(\frac{R_*}{r}\right)^2 + T_0^4\right]^{1/4} \tag{3}$$

where r is the cylindrical distance from the star, $T_0 = 7$ K is a constant, and $\phi = 0.05$ is the angle between the incident radiation and disk surface ('flaring' angle). The sound speed c_s is defined as $\sqrt{k_B T/\mu m_H}$, where k_B is the Boltzmann constant, $\mu = 2.3$ is the mean molecular weight of the gas, and m_H is the mass of hydrogen atom. Our neglect of heating due to viscous dissipation leads to a modest underestimation of the temperature in the inner regions of the disk but greatly simplifies the determination of the temperature structure. We note that accounting for the varying opacities that arise from the growth and transport of grains into the temperature profile is outside the scope of this paper (see, e.g. Savvidou et al. 2020, for recent attempts in this direction).

The gas surface density (Σ_g) is evolved following the fluid equations of viscously spreading accretion disk (Lynden-Bell & Pringle 1974)

$$\frac{\partial \Sigma_g}{\partial t} = \frac{3}{r}\frac{\partial}{\partial r}\left[r^{1/2}\frac{\partial}{\partial r}\left(\nu \Sigma_g r^{1/2}\right)\right] \tag{4}$$

whose self-similar solution (at time zero) is used to set the initial surface density profile for our calculation:

$$\Sigma_g(r) = C\left(\frac{r}{r_c}\right)^{-p} \exp\left[-\left(\frac{r}{r_c}\right)^{2-p}\right] \tag{5}$$

where C is a constant to be normalized by the assumed disk gas mass, ν is the kinematic viscosity with a power law radial profile ($\nu = \nu_c (r/r_c)^p$), and r_c is a characteristic radius of the disk. Following Birnstiel et al. (2012), we set $p = 1$ and $r_c = 200$ au in our work. The viscosity $\nu = \alpha_t c_s H_g$ is parameterized using the Shakura-Sunyaev turbulence parameter α_t (Shakura & Sunyaev 1973), the sound speed c_s, and the gas scale height $H_g = c_s/\Omega$, where Ω is the Keplerian frequency.

The dynamics of dust is modelled using just two representative grain sizes in the disk (hence the name `twopoppy`): the spatially and temporally constant monomer size a_0 and a large grain size a_1 that depends on time and location in the disk. We fix $a_0 = 0.005\mu$m to align this variable with the minimum grain size in the ISM size distribution. These small grains rapidly coagulate to form agglomerates that are many orders of magnitude larger in size. Their growth is limited by processes such as turbulent fragmentation and radial drift. These limiting sizes are what set the value of a_1 as a function of time and r and they are discussed in greater detail later in this section.

Splitting the dust population into two allows us to capture the qualitatively different dynamical behavior of large and small grains. Small grains are well coupled to the gas and are unable to maintain large relative velocities with respect to the gas. On the other hand, large grains are slightly decoupled from the gas and respond to pressure gradients on relatively short timescales. The total surface dust density (Σ_d) is the sum of the surface density of small (Σ_0) and large (Σ_1) grains and can consequently be modelled using a single advection-diffusion equation:

$$\frac{\partial \Sigma_d}{\partial t} + \frac{1}{r}\frac{\partial}{\partial r}\left[r\left(\Sigma_d \bar{u} - D_{gas}\Sigma_g \frac{\partial}{\partial r}\left(\frac{\Sigma_d}{\Sigma_g}\right)\right)\right] = 0. \tag{6}$$

Here, $\bar{u}$ is the mass weighted radial velocity of dust grains and D_{gas} is the gas diffusivity. A derivation of this equation is available in the appendix of Birnstiel et al. (2012).

The Stokes number St is dust grain stopping time under gas aerodynamic drag in units of local orbital time. Dust grains smaller than the gas particle mean free path are in Epstein drag regime and their Stokes numbers follow

$$\mathrm{St} = \frac{\pi}{2}\frac{a\rho_s}{\Sigma_g}. \tag{7}$$

Detailed dust growth and evolution simulations indicate that grains will continue to grow until they reach a size (St $\sim$ $0.1-1$) where fragmentation due to collisions and/or loss to radial drift become significant (e.g. Brauer et al. 2008; Birnstiel et al. 2010). For grains in this size range, velocity differences between grains due to turbulence become larger ($\Delta u \propto \sqrt{\mathrm{St}}$, Ormel & Cuzzi 2007) and collisions are more likely to lead to fragmentation instead of growth. This limits the maximum Stokes number and corresponding size a_{frag} that the grains can reach:

$$\mathrm{St}_{frag} = \frac{1}{3\alpha_t}\frac{v_{frag}^2}{c_s^2} \tag{8a}$$

$$a_{frag} = \frac{2}{3\pi}\frac{\Sigma_g}{\rho_s \alpha_t}\frac{v_{frag}^2}{c_s^2} \tag{8b}$$

where v_{frag} is the fragmentation velocity of dust grains.

The rate of radial drift is maximized for particles marginally coupled to gas (St $\sim$ 1) (Weidenschilling 1977; Chiang & Youdin 2010):

$$u_{drift} = -\frac{2u_\eta}{\mathrm{St} + \mathrm{St}^{-1}} \tag{9}$$

where $u_\eta = -\gamma c_s^2/2v_K$ is the drift velocity, v_K is the Keplerian velocity, and $\gamma = |\mathrm{d}\ln P\,/\,\mathrm{d}\ln r|$ is the power law index characterising the dependence of pressure on distance from the star. In some regions of the disk, particles may drift radially faster than they can grow to the size at which fragmentation dominates. In these regions, the radial drift sets an upper limit on the particle size $a_{\rm drift}$:

$$a_{\rm drift} = \frac{2}{\pi}\frac{\Sigma_{\rm d}}{\rho_s \gamma}\frac{v_K^2}{c_s^2} \tag{10}$$

At early times in the disk evolution, the particle growth rate can also be a limiting factor for grain growth and set the maximum particle size. This can be true even at late times in the outer disk where the growth timescales ($\tau_{\rm grow} \simeq 1/\epsilon\Omega$) are longer. In the two population model for dust evolution, the large grain size a_1 is fixed to a fraction of the maximum grain size that is determined by calibrating the `twopoppy` model to the full simulations (Birnstiel et al. 2012). The maximum particle size limit therefore plays an important role in determining the dynamics of the large grains in the disk. Since most of the dust mass tends to be concentrated in the largest grains, which are also the most susceptible to radial drift, the dust-to-gas ratio of the disk can evolve significantly over time.

The turbulence parameter $\alpha_{\rm t}$ and the fragmentation velocity $v_{\rm frag}$ are two of the most important parameters for determining the maximum particle size. The classically quoted range of values for $\alpha_{\rm t}$ is $10^{-4} - 10^{-2}$ (e.g. Turner et al. 2014). However, recent studies of line broadening and dust settling in protoplanetary disks suggest that $\alpha_{\rm t}$ is closer to the lower end of this range (Mulders & Dominik 2012; Pinte et al. 2016; Flaherty et al. 2015, 2017, 2018). We therefore adopt $\alpha_{\rm t} = 10^{-3}$ for our baseline model and comment on the consequences of varying $\alpha_{\rm t}$ in § 3.3.[2]

Both theoretical studies and experiments have long suggested a significant difference between the fragmentation velocities of ice-free and icy dust (Poppe et al. 2000; Blum & Wurm 2008; Wada et al. 2013; Gundlach & Blum 2015). Most commonly, ice-free silicate dust is assumed to have a fragmentation velocity of 1 m/s, while icy grains have a fragmentation velocity closer to 10 m/s (e.g. Birnstiel et al. 2010; Pinilla et al. 2016; Drążkowska & Alibert 2017). Such a difference in fragmentation velocity would lead to an abrupt change in the dust emission spectral index at water ice line (Banzatti et al. 2015) and there is observational evidence to support the occurrence of this phenomenon (Cieza et al. 2016). This increase in fragmentation velocity for dust exterior to the water ice line has also been invoked to explain the architecture of the solar system and exoplanetary systems (e.g. Morbidelli et al. 2015; Venturini et al. 2020) as well as planetesimal formation (Drążkowska & Alibert 2017).

Despite this apparent consensus, recent theoretical and laboratory studies have begun to cast doubt on this story. Previous studies attributed the change in $v_{\rm frag}$ to an order of magnitude difference in the surface energies of icy and ice-free dust grains, but recent experimental work now suggests that their surface energies may in fact be quite similar (Gundlach et al. 2018; Steinpilz et al. 2019). Other studies conclude that the fragmentation velocity might exhibit a more complicated and non-monotonic dependence on temperature (e.g. Gundlach et al. 2018; Musiolik & Wurm 2019), and this topic remains an area of active debate in the community (e.g. Kimura et al. 2020). In this study we adopt the standard values of 1 m/s for ice-free and 10 m/s for icy grains for our baseline case, as these are close to the values derived from dynamical collision experiments. We assume that the ice line is located where the disk temperature drops below approximately $T = 200$ K and we use Gaussian convolution to smoothly increase $v_{\rm frag}$ from 1 m/s at 250 K to 10 m/s at 150 K (e.g. Birnstiel et al. 2010). In § 3.3, we also present alternative models where we vary the value of $v_{\rm frag}$ both within and beyond the ice line and show that our results are qualitatively similar for a significant part of the plausible parameter space.

We utilize the approximations from Birnstiel et al. (2015) that are implemented in `twopoppy` to reconstruct the full grain size distribution in the protoplanetary disk, which we need in order to calculate the corresponding dust opacity. These approximations match the detailed simulations reasonably well, but can underestimate the number density of small grains. Although this will affect the opacity of the disk at short wavelengths (e.g., $\sim 1\ \mu$m), we find that it only has a modest effect on the Rosseland mean opacity. We quantify this effect by comparing the mean opacity from this approximate method to the more accurate coagulation-fragmentation models from Birnstiel et al. (2011) in the fragmentation dominated region of the protoplanetary disk and find that the opacity from the approximate method is a factor of two smaller. In regions dominated by radial drift, a change in the assumed power law index for the size distribution can also affect the number of small particles. However, since radial drift tends to dominate in the outer colder parts of the disk, the mean opacity in this region is dominated by slightly larger grains ($\sim 100\mu$m), which have a more robustly determined number density.

So far, we have discussed grain sizes, distributions, and opacities in the framework of a vertically integrated (2D) disk. If we wish to explore the 3D disk structure, we can extend these 2D models by using some reasonable approximations to calculate the density of dust and gas as a function of height from the midplane. This exercise is particularly valuable for planet formation models because growing protoplanets might not accrete most of their gas from the midplane (see § 4). We assume a Gaussian vertical profile with a scale height $H_g(r) = c_s/\Omega$ for the gas. The midplane gas density is then given by $\rho_{\rm g,0} = \Sigma_g/\sqrt{2\pi}H_g$ (Equation 7, which

[2] We note that we use the same α_t for both the global disk gas evolution and the turbulent stirring of dust. In reality, these two can be different (see, e.g., Carrera et al. 2017; Drążkowska & Alibert 2017).

gives the expression for St in the midplane, also used this assumption). Dust sediments towards the midplane and is carried upward by turbulent diffusion so its vertical density distribution is significantly different from that of the gas. We use the expression for the steady-state vertical distribution of dust derived by Fromang & Nelson (2009):

$$\rho_{\rm d}(z,a) = \rho_{\rm d,0} \exp\left[-\frac{{\rm St}_0}{\alpha_{\rm t}}\left(\exp\left(\frac{z^2}{2H_{\rm g}^2}\right)-1\right)-\frac{z^2}{2H_{\rm g}^2}\right] \quad (11)$$

where $\rho_{\rm d,0}(a)$ is the dust density and ${\rm St}_0(a)$ is the Stokes number in the midplane for a particular grain size.

2.3. *Calculation of dust opacity*

The composition of dust grains in protoplanetary disks is a topic of active research (see recent review by Oberg & Bergin 2020). We adopt the grain composition prescribed in the DSHARP survey papers and use the publicly available tools generously provided by the survey team for the calculation of grain properties (Birnstiel et al. 2018). The DSHARP composition mixture consists of water ice (optical properties from Warren & Brandt 2008), 'astrosilicates' (Draine 2003), and refractory organics and troilite (FeS) (Henning & Stognienko 1996). We adopt the same grain composition for the entire disk, as removing water from our mixture has only a small effect ($\lesssim$ 15%, accounting for the difference in grain densities and optical properties but keeping the grain size distribution fixed) on the calculated opacity. Our simulations also do not account for the effect of condensation/sublimation on grain size and mass for particles moving across the ice line when calculating the grain size distribution. For the adopted DSHARP mixture, water's sublimation would reduce dust mass only by 20% within the ice line. Accounting for the reduced mass and increased density of ice free grains would reduce the grain size by $\sim$ 15%, which will have some effect on their dynamics. However, these effects are negligible compared to the other sources of uncertainty in our model.

We use Mie theory to calculate the dust opacity. Our Mie code is publicly available as part of `PLATON` (Zhang et al. 2019, 2020), which uses the algorithm outlined by Kitzmann & Heng (2018). For particle sizes and wavelengths for which the full Mie treatment is impracticable, we resort to widely used approximations. We use the geometric optics limit to calculate the absorption cross-section of particles for which $|m|x > 1000$ and $|m-1|x > 0.001$, where m is the complex refractive index of the particle and $x = 2\pi a/\lambda$ is the size parameter (here a being the particle size and λ being the wavelength, van de Hulst 1957). Specifically, we use the approximation described in Laor & Draine (1993), which uses the extinction coefficient calculated using Rayleigh-Gans approximation ($Q_{\rm RG}$) to obtain the extinction coefficient in the geometric optics limit ($Q_{\rm ext}$):

$$Q_{\rm ext} \approx \frac{Q_{\rm RG}}{(1+0.25Q_{\rm RG}^2)^{1/2}} \quad (12a)$$

$$Q_{\rm RG} = \frac{32|m-1|^2x^4}{27+16x^2} + \frac{8}{3}{\rm Im}(m)x \quad (12b)$$

where Im(m) is the imaginary part of the refractive index.

Once we have calculated the absorption coefficient for different particle sizes a and wavelength λ, the wavelength dependent opacity $\kappa_{\lambda,a}$ for each particle size per gram of dust is given by:

$$\kappa_{\lambda,a} = \frac{\pi a^2 Q_{\rm ext}(\lambda,a)}{4\pi\rho_s a^3/3} \quad (13)$$

To calculate the opacity per gram of dust in the protoplanetary disk, we need the normalized size distribution of the grains at a specific location. We utilize the mass density distribution of dust $\Sigma_{\rm d}(r,a)$, calculated in logarithmic bins of grain size using `twopoppy`. The opacity per gram of dust in the protoplanetary disk is then obtained using:

$$\kappa_\lambda = \frac{\int \kappa_{\lambda,a}\Sigma_{\rm d}(r,a)\ {\rm d}\ \ln a}{\int \Sigma_{\rm d}(r,a)\ {\rm d}\ \ln a} \quad (14)$$

This wavelength dependent opacity is used to calculate the Rosseland mean opacity per gram of dust:

$$\frac{1}{\kappa_R} = \frac{\int_0^\infty (1/\kappa_\lambda)(\partial B_\lambda/\partial T)d\lambda}{\int_0^\infty (\partial B_\lambda/\partial T)d\lambda} \quad (15)$$

where B_λ is the Planck function and T is the temperature used in our protoplanetary disk model. To obtain the Rosseland mean opacity per gram of protoplanetary disk material, we multiply the κ_R obtained above by the local dust-to-gas ratio $\epsilon = \Sigma_d(r)/\Sigma_g(r)$ of the disk. We do not include the gas opacity in our calculations, as the dust opacity dominates even in the regions with the lowest dust-to-gas ratio and/or the largest particle sizes (see § 4.1).

3. DUST OPACITY IN PROTOPLANETARY DISKS

3.1. *Opacity from a simulated size distribution*

In this section, we focus on quantifying the changes in the dust opacity due to location-dependent variations in the dust size distribution. We show the full radially-varying `twopoppy` size distribution in the top panel of Figure 1 and the resulting Rosseland mean opacity per gram of dust in Figure 2. The size distribution in the inner 10 au is dominated by coagulation-fragmentation equilibrium, while the increase in $v_{\rm frag}$ beyond the water ice line at $\sim$ 1 au manifests as an increase in the maximum grain size ($a_{\rm frag} \propto v_{\rm frag}^2$ from Equation 8). Since larger grains contain more mass and the size distribution is slightly top-heavy, this increase

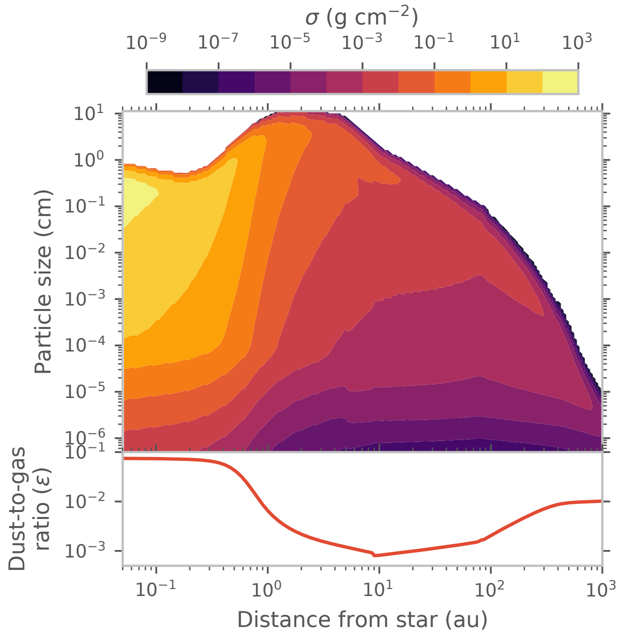

Figure 1. Size distribution and dust-to-gas ratio (ϵ) at time t = 1 Myr for a `twopoppy` simulation with variable $v_{\rm frag}$ and $\alpha_{\rm t} = 10^{-3}$.

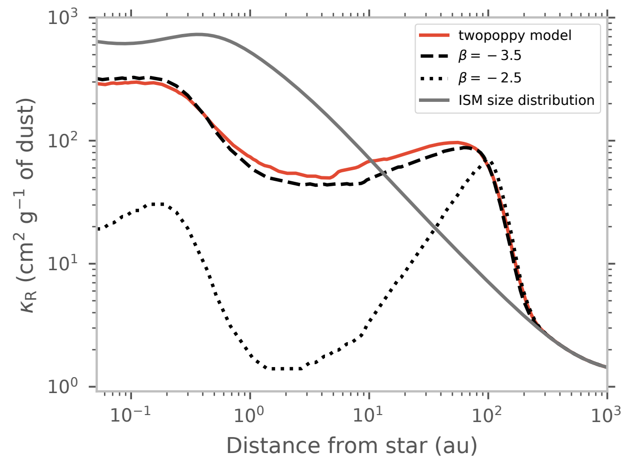

Figure 2. Rosseland mean opacity per gram of dust as a function of distance from the star at time t = 1 Myr. We adopt $\alpha_{\rm t} = 10^{-3}$ and a variable $v_{\rm frag}$ that changes across the water ice line for our `twopoppy` model. For the power law distributions, $a_{\rm max}$ is set by the location specific maximum grain size calculated from `twopoppy`, which is given by Equation 8 (fragmentation-limited), Equation 10 (drift-limited), or the growth-timescale limit.

in $v_{\rm frag}$ causes the surface density of small grains ($\lesssim 10\mu$m) to decrease by multiple orders of magnitude. Because these grains contribute significantly to $\kappa_{\rm R}$, this change is responsible for the factor of ~ 5 decrease in the simulated $\kappa_{\rm R}$ shown in Figure 2. Beyond ~ 10 au, the maximum grain size is set by radial drift of the large grains instead of fragmentation as particles drift inward before they can grow to the fragmentation barrier. Without fragmentation to replenish the supply of small grains, the size distribution in this region becomes more top heavy relative to the distribution produced by the coagulation-fragmentation equilibrium in the inner disk. $\kappa_{\rm R}$ in this cold outer disk region is dominated by larger grains ($\sim 100\ \mu$m) that are relatively abundant, leading to a modest increase in the simulated $\kappa_{\rm R}$ as shown in Figure 2.

In Figure 2, we compare $\kappa_{\rm R}$ for size distribution simulated by `twopoppy` at time t = 1 Myr with three different grain size distributions: the ISM size distribution ($\beta = -3.5, a_{\rm max} = 0.25\mu$m) and power law distributions with β of either -2.5 or -3.5 and maximum particle sizes set to the fragmentation (Eq. 8), radial drift (Eq. 10), or growth-timescale limits, as appropriate. We find that the dust opacity for the simulated size distribution differs significantly from that of the ISM size distribution (see also Savvidou et al. 2020). The opacity of the ISM size distribution only varies as a consequence of the decreasing temperature in the disk. In contrast, the simulated size distribution reflects radially varying grain growth and transport processes in the disk. It is noteworthy that a power law distribution with $\beta = -3.5$ (same as that of the ISM) and $a_{\rm max}$ set by the relevant physics of fragmentation and radial drift yields a $\kappa_{\rm R}$ profile that is in good agreement with the simulated results.

We illustrate the effect of the maximum grain size $a_{\rm max}$ and the power law index β on $\kappa_{\rm R}$ in Figure 3. The smallest value of $a_{\rm max}$ shown on the plot corresponds to the ISM size distribution. For top heavy distributions with $\beta > -4$, most of the mass is concentrated in the larger dust grains. Increasing $a_{\rm max}$ therefore redistributes dust mass from smaller grains to larger grains, reducing the total number of small grains. This can significantly alter the overall opacity of the dust: if we compare $\kappa_{\rm R}$ for $a_{\rm max} = 0.1$ cm (which is more typical for dust in a disk) and $\beta = -3.5$ with the equivalent ISM value, it is almost 20 times larger at 10 K. Conversely, this same depletion of smaller grains for $a_{\rm max} = 0.1$ cm means that $\kappa_{\rm R}$ is half the corresponding ISM value at 1000 K. Using a realistic $a_{\rm max}$ for the power law size distribution of dust in a protoplanetary disk therefore leads to a reduced $\kappa_{\rm R}$ in the hotter inner disk and an enhanced $\kappa_{\rm R}$ in the colder outer disk.

In contrast to this result, the opacity from a power law size distribution with $\beta = -3.5$ and $a_{\rm max}$ set by Equations 8 and 10 and growth timescale $\tau_{\rm grow}$ provides a relatively good match to the opacity from the full simulated size distribution. The power law size distribution with $\beta = -2.5$ does not perform as well; this is due to the top heaviness of the $\beta = -2.5$ size distribution, which leads to a dramatic depletion in the number of small grains. Since the small grains that contribute most significantly to $\kappa_{\rm R}$ at the protoplanetary disk temperatures are absent, the opacity for $\beta = -2.5$ is $\gtrsim 1$ order of magnitude lower than that for our `twopoppy` simulation. These results for different β values are similar to previous findings

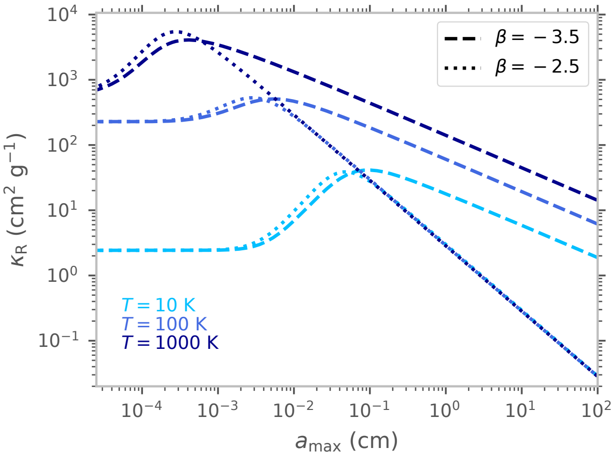

Figure 3. Rosseland mean opacity per gram of dust for a power law grain size distribution with $\beta = -3.5$ and -2.5 and three different temperatures. The lowest value of $a_{max} = 0.25\mu$m on this plot is the commonly adopted value for the ISM size distribution.

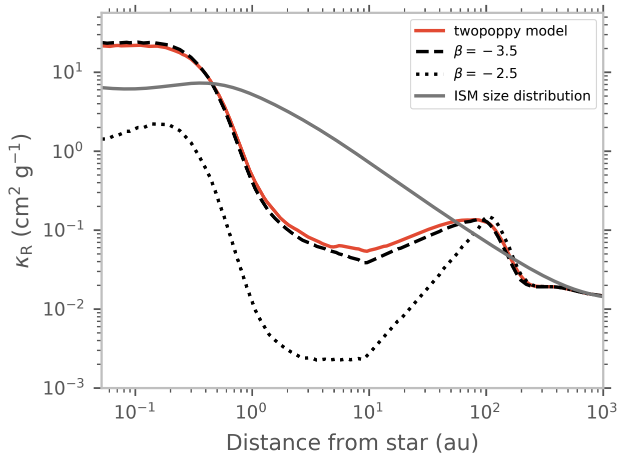

Figure 4. Rosseland mean opacity per gram of protoplanetary disk material at time $t = 1$ Myr and for a variable v_{frag} and $\alpha_t = 10^{-3}$. This plot is similar to Figure 2 except that the opacity per gram of dust is here multiplied by the radially-varying dust-to-gas ratio. For the ISM size distribution, the dust-to-gas ratio is assumed to be 0.01 everywhere.

for the dust opacity at specific wavelengths (e.g. D'Alessio et al. 2001).

3.2. *Opacity from a radially varying dust-to-gas ratio*

Now that we have explored the effect of a radially varying dust size distribution on the Rosseland mean opacity per gram of dust, we can account for the radially varying dust-to-gas ratio ϵ. As noted earlier, we assume that the contribution of the gas opacity to κ_R is negligible. The dust-to-gas ratio (or metallicity) is typically fixed to a single global value (e.g. Bitsch et al. 2015; Mordasini 2018). However, this ratio can change radially as dust abundance evolves. Here we use our simulations to explore how the distribution of dust evolves in time as a function of assumed disk properties such as the turbulence strength α_t and v_{frag}.

We begin our simulation with a globally uniform $\epsilon = 0.01$ and show the resulting vertically integrated dust-to-gas ratio ($\epsilon = \Sigma_d/\Sigma_g$) at time $t = 1$ Myr for our fiducial model in the bottom panel of Figure 1. As grains begin to grow and their Stokes number increases, they face a stronger headwind from the gas and start drifting towards the star. In the outermost regions of the disk ($\gtrsim 100$ au), the grain growth rate is so slow that particles do not reach the drift barrier, i.e. they do not drift very efficiently. ϵ far out does not evolve significantly and only decreases slowly as one moves closer to 100 au. Between ~ 10 and 100 au, grains drift inward faster than they can grow, causing the dust-to-gas ratio to decrease over time. In the inner disk, orbital timescales are shorter and grain growth is rapid. This means that grains reach the fragmentation barrier before they can drift appreciably. For a fixed v_{frag} and α_t, the Stokes number of the largest grains also decreases as one moves closer to the star (see Eq. 8). This means that grains in the fragmentation-dominated inner disk are better coupled to the gas, and the dust-to-gas ratio does not decline as rapidly as in the drift-dominated outer disk region. In fact, the dust-to-gas ratio in the inner disk may even be enhanced by the migration of dust from the outer disk.

Depending on the magnitude of the velocity offset, the change in v_{frag} across the ice line can have a dramatic effect on the dust dynamics. When large grains drifting inward from the outer disk cross the ice line they lose their ice and their fragmentation velocity decreases to the value characteristic of ice-free dust. Post-fragmentation grains are therefore smaller and their St is reduced, slowing their inward drift and causing a pile up of dust inside the ice line. The magnitude of this effect can be quite large: for a factor of 10 decrease in v_{frag} across the ice line, the St of the largest grains decreases by almost two orders of magnitude ($\mathrm{St}_{frag} \propto v_{frag}^2$). As shown in Figure 1 this enhances the dust-to-gas ratio ϵ within ~ 1 au by almost an order of magnitude at $t = 1$ Myr relative to the starting ϵ of 0.01. Conversely, most of the disk beyond 1 au is significantly depleted of dust with $\epsilon \sim 10^{-3}$ for a large part of the outer disk. The effect of radial drift, fragmentation, and a change in v_{frag} across the ice line on dust dynamics have been extensively described in Birnstiel et al. (2010); Pinilla et al. (2017), and we refer the reader to these studies for a comprehensive exploration of this topic.

We can use this radially and temporally varying dust-to-gas ratio to update our calculation of the Rosseland mean opacity of the disk. Figure 4 shows κ_R per gram of protoplanetary disk material for our simulated size distribution. This plot is the same as Figure 2 except that the κ_R profiles shown in that figure are now multiplied by the dust-to-gas ratio. We plot the ISM κ_R assuming a constant dust-to-gas ratio of 0.01, in

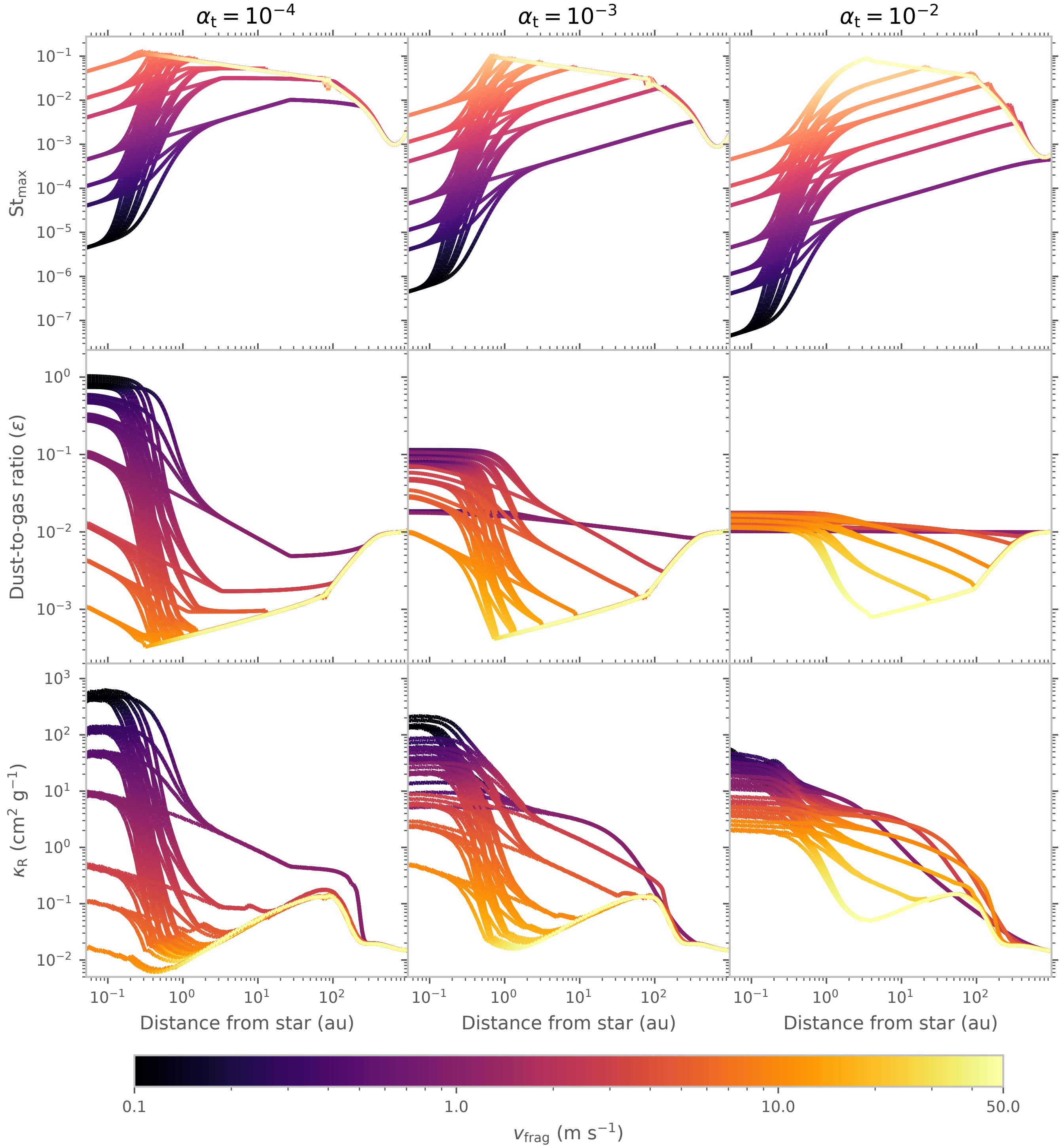

Figure 5. The Stokes number of the largest grain size ($\mathrm{St_{max}}$), dust-to-gas ratio (ϵ), and Rosseland mean opacity per gram of protoplanetary disk material for a range of fragmentation velocities within and beyond the water snow line as well as three different turbulence strengths (α_t).

order to better illustrate the differences between our model and the widely used ISM opacity model. Within the ice line, the dust-to-gas ratio is enhanced by a factor of ten relative to the ISM model, which partially compensates for the reduction in opacity due to the increased grain sizes (Figure 2). As we move beyond the ice line, the decreasing quantity of dust and increasing concentration of dust mass in larger particle sizes lead to a steep decline in the opacity. Our κ_R between $\sim$1 and $\sim$10 au is smaller than the ISM value by more than a factor of ten.

3.3. *Dependence on the assumed fragmentation velocity and turbulence strength*

Our fiducial model predicts that the dust opacity will decrease by more than two orders of magnitude as we move outside the ice line. However, the magnitude of this gradient depends strongly on the absolute and relative efficiency of dust transport in the inner and outer disk. The transition from the fragmentation-dominated to the drift-dominated regime can be expressed as a function of the fragmentation velocity $v_{\rm frag}$ and the turbulence strength α_t (e.g. Birnstiel et al. 2015):

$$\frac{v_{\rm frag}^2}{v_K^2} > \frac{3\alpha_t \epsilon}{\gamma} \tag{16}$$

This transition also depends on the Keplerian velocity v_K, the dust-to-gas ratio ϵ, and $\gamma = |{\rm dln}P/{\rm dln}r|$. All of these quantities can vary as a function of r (although we assume α_t is constant in our work) and in regions where this inequality is satisfied, the disk becomes drift-dominated. Since α_t and $v_{\rm frag}$ are not known a priori, we run a grid of models over $\alpha_t \in [10^{-4}, 10^{-3}, 10^{-2}]$ where $\alpha_t = 10^{-3}$ is our fiducial, and $v_{\rm frag} = 0.1-10$ m s^{-1} for ice-free grains and $1-50$ m s^{-1} for icy grains (e.g. Blum & Wurm 2008; Gundlach & Blum 2015). We consider all possible combinations of these two fragmentation velocities as long as they meet the requirement that $v_{\rm frag}$ for icy grains is greater than or equal to $v_{\rm frag}$ for ice-free grains [3].

Figure 5 shows the Stokes number of the largest grains $\rm St_{max}$, the dust-to-gas ratio ϵ, and the disk's Rosseland mean opacity κ_R for this grid of models. As α_t decreases, we find that ϵ varies more strongly with orbital distance: a consequence of the difference in the absolute values of $\rm St_{max}$ for different α_t. For $\alpha_t = 10^{-4}$, $\rm St_{max} \gtrsim 10^{-2}$ between $\sim$1 and 100 au. A larger Stokes number beyond the ice line leads to more efficient inward drift of dust from the outer to the inner disk. For lower α_t, the transition to the drift-dominated region also happens closer in to the star (see Equation 16 above), creating a 'kink' in $\rm St_{max}$ and ϵ profiles (e.g. at 10 au in our fiducial model, see bottom panel of Figure 1). In the outer disk, all models that transition to the drift-dominated regime converge to similar values for $\rm St_{max}$ and ϵ. For $\alpha_t = 10^{-2}$ this transition moves outside $\sim$ 100 au for most models, causing the disk to be globally fragmentation-dominated. As a result, $\rm St_{max}$ has a lower value throughout the disk and dust migration is suppressed.

The high St realized in low α_t disk that aids the radial transport of dust grains in the outer disk begins to diminish the dust pile-up in the inner disk. Since $\rm St_{frag} \propto \alpha_t^{-1}$, $\rm St_{max}$ in the inner disk is larger for lower α_t. These high-St grains continue to rapidly drift in through the inner edge of the disk and shuttle towards the central star, becoming lost from the disk and essentially erasing initial pile-ups. Maximizing the dust-to-gas ratio and consequently the opacity gradient in the radial direction requires an intermediate value of α_t which in turn is dependent on $v_{\rm frag}$.

Larger differences in the $v_{\rm frag}$ values for icy and ice-free grains lead to a larger change in $\rm St_{max}$ across the ice line. This in turns results in a depletion of dust in the outer disk and a pile up of dust in the inner disk, leading to larger opacity contrast between the inner and the outer disk (see Figure 6), as long as the value of α_t does not nullify these effects by either producing globally low values of $\rm St_{max}$ (well coupled dust and little dust transport) or large values of $\rm St_{max}$ within the ice line (dust drifts towards the star and does not pile up). However, when $v_{\rm frag}$ is large everywhere in the disk (e.g. 10 m/s for ice-free grains and 50 m/s for icy grains), particles will have large $\rm St_{max}$ and will rapidly drain onto the star.

To simplify comparisons between models, in Figure 6 we focus on the ratio of the disk opacity κ_R at 0.1 au and 5 au. These distances are chosen to best capture the opacity contrast for the full set of disk models; they are also approximately where sub-Neptunes and gas giants are most numerous, respectively. We find that there is a large range of choices for $v_{\rm frag}$ and α_t that lead to opacity contrasts that are equal to or larger than the one in our fiducial model. Decreasing α_t enlarges $\rm St_{max}$ and accelerates the grain radial transport, enhancing the contrast in the opacity across the snow line. Larger differences in $v_{\rm frag}$ between icy and ice-free grains also produce greater opacity contrasts as they lead to a strong gradient in dust transport efficiency across the snow line.

The opacity contrast with increasing $v_{\rm frag}$ for icy grains saturates at a value that depends on the $v_{\rm frag}$ for ice-free grains. This is most evident in the lower α_t models and occurs because $\rm St_{max}$ and ϵ converge to similar values in the outer disk (Figure 5). Beyond this limit, increasing the $v_{\rm frag}$ for icy grains does not lead to an increase in the Stokes number of the largest grains in the outer disk but instead simply pushes the transition from fragmentation-dominated regime to drift-

[3] We note that the `twopoppy` models are calibrated with the full numerical models for a smaller range of $v_{\rm frag}$ (1 – 10 m/s) than we study here. However, this should not be a major concern as the underlying collisional outcome model is the same.

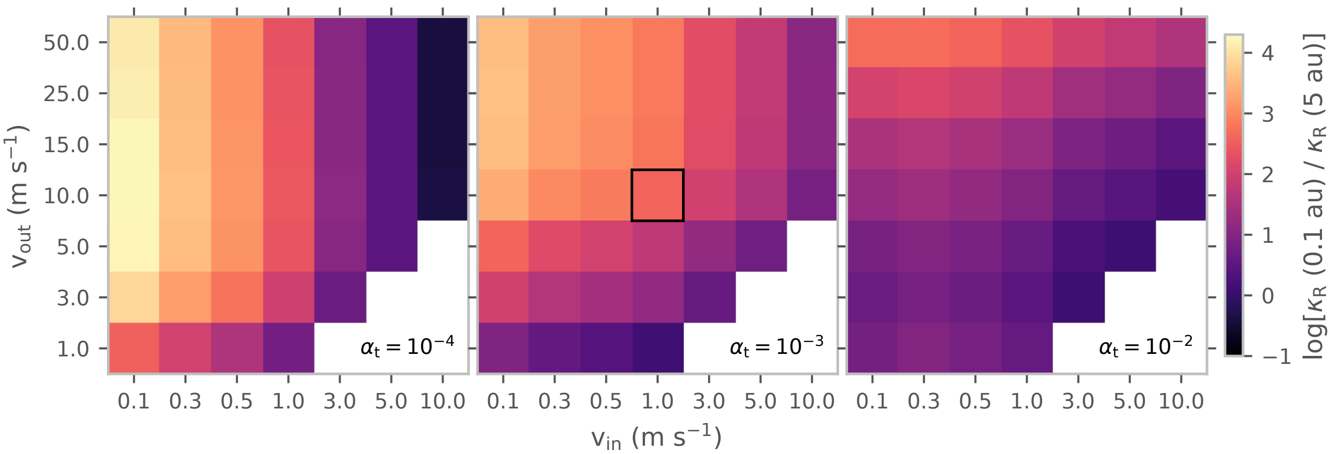

Figure 6. Ratio of the Rosseland mean opacity per gram of protoplanetary disk material at 0.1 au and 5 au after 1 Myr of evolution. The axes labels $v_{\rm in}$ and $v_{\rm out}$ stand for the fragmentation velicity within and beyond the ice line. Our fiducial model is outlined with a black square.

dominated regime inward. This limits the supply of dust from the outer disk and causes the opacity contrast to saturate at a fixed $v_{\rm frag}$ for ice-free grains.

Recent observations of protoplanetary disks appear to favor values for $\alpha_{\rm t}$ that are lower than 10^{-2} (e.g. Pinte et al. 2016; Flaherty et al. 2018). As we discussed earlier, it is less clear how large the difference in $v_{\rm frag}$ for icy and ice-free dust grains may be (Gundlach et al. 2018; Steinpilz et al. 2019; Kimura et al. 2020). However, our parameter space exploration suggests that there are a wide range of plausible scenarios that can lead to a large opacity gradient between the inner and outer disk regions.

3.4. *Dust opacity in a 3D disk*

So far, we have only considered vertically integrated disk models. In this section we examine the vertical structure of the dust distribution and its potential importance for planet formation (e.g., polar accretion of gas onto planetary cores; Ormel et al. 2015; Fung et al. 2015; Cimerman et al. 2017; Lambrechts & Lega 2017) and modelling protoplanetary disks. The vertical structure of gas and dust is controlled by a complicated coupling between the disk temperature, opacity, and turbulence. Self-consistently taking these couplings into account is beyond the scope of our study; instead, we utilize a simple vertically isothermal disk model. Even with this simplification, our model produces a non-uniform vertical distribution of dust grains.

We use the prescribed radial temperature structure from Equation 3 and assume a vertically isothermal disk structure in order to calculate the vertical structure of the dust and gas. Under this assumption, the gas density $\rho_g \propto e^{-z^2/H_{\rm gas}^2}$ where z is the height from the midplane and $H_{\rm gas} = c_s/\Omega$ is the gas disk scale height. For the vertical dust density distribution, we utilize the expression obtained by Fromang & Nelson (2009) for the steady-state distribution of dust (Equation 11).

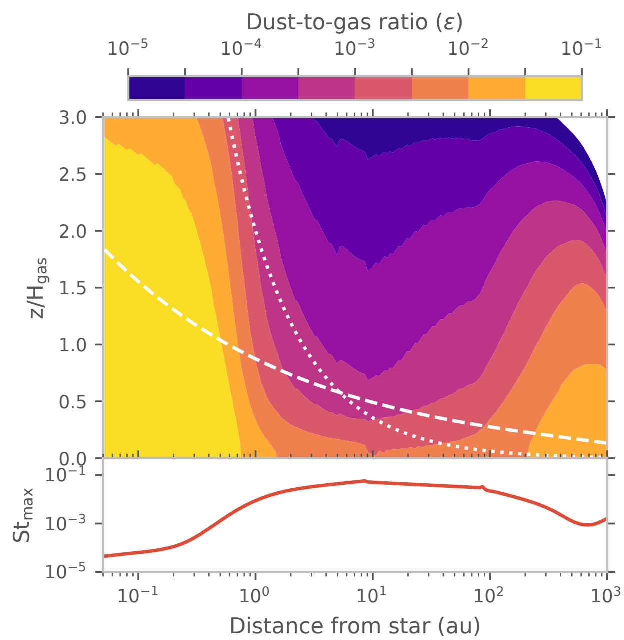

Figure 7. The top panel shows the dust-to-gas ratio ϵ as a function of height above the midplane z and distance from the star after 1 Myr of evolution. The white dashed and dotted lines mark the height of the Hill radius $R_{\rm Hill}$ and Bondi radius $R_{\rm Bondi}$ of a 15 $M_\oplus$ planet respectively. The bottom panel shows the midplane Stokes number of the largest grains present in the disk at $t = 1$ Myr. Well coupled grains within the ice line lead to efficient vertical mixing of grains and hence a weak dependence of ϵ on z. Beyond the ice line, large grains that dominate the dust mass settle close to the midplane, which leads to a strong decline in ϵ as a function of z.

We calculate the 3D dust density $\rho_d(z, a)$ for logarithmically binned grain sizes and sum it to obtain the total dust density $\rho_d(z)$. The dust-to-gas ratio ϵ is then simply calculated as ρ_d/ρ_g.

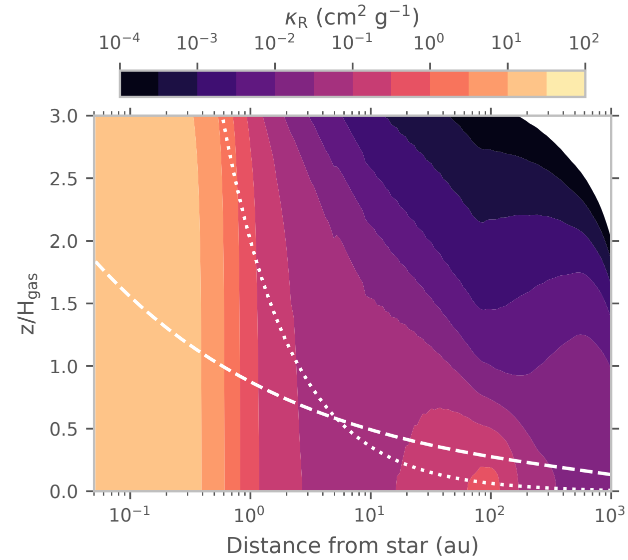

Figure 8. Rosseland mean opacity per gram of protoplanetary disk material as a function of height above the midplane z and distance from the star after 1 Myr of evolution. The white dashed and dotted lines mark the height of the Hill radius $R_{\rm Hill}$ and Bondi radius $R_{\rm Bondi}$ of a 15 $M_\oplus$ planet respectively. Vertically well mixed dust within the ice line leads to little variation in κ_R as a function of z. Grain settling and a strong decline in ϵ with z leads to a gradient in κ_R as a function of z beyond the ice line.

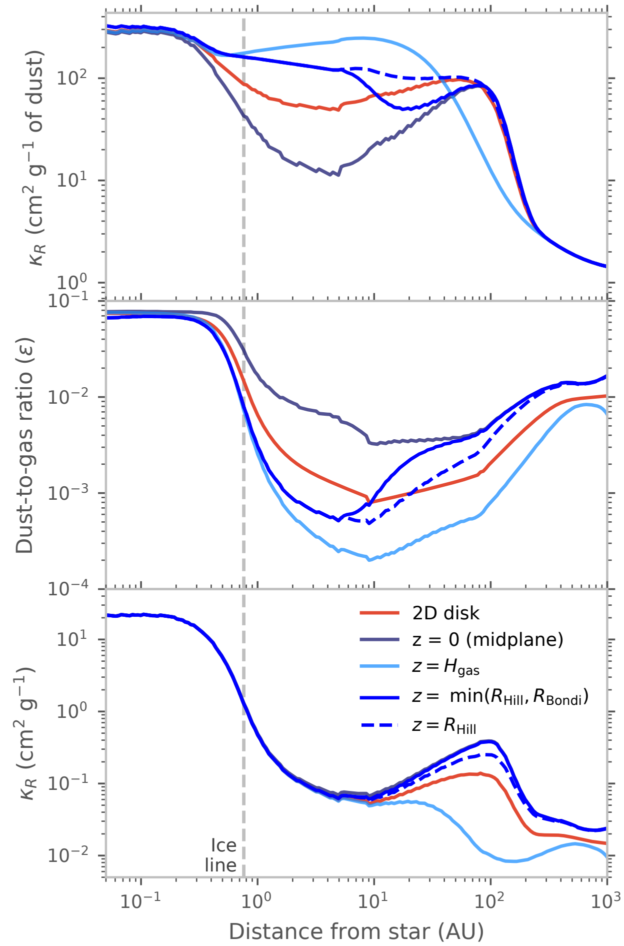

Figure 9. A comparison of the Rossleand mean opacity per gram of dust, dust-to-gas ratio ϵ, and Rosseland mean opacity per gram of protoplanetary disk material κ_R for our fiducial 2D disk integrated model and our 3D disk model after 1 Myr of evolution. We plot the values of these quantities in the disk midplane ($z = 0$), a single gas scale height above the midplane ($z = H_{\rm gas}$), and at heights of a 15 $M_\oplus$ planet's $R_{\rm Hill}$ and min($R_{\rm Hill}, R_{\rm Bondi}$) above the midplane. The water ice line is marked with a dashed grey line.

The top panel in Figure 7 shows the resulting dust-to-gas ratio ϵ as a function of z and distance from the star for our fiducial model at a disk age of 1 Myr. The differences in ϵ as a function of z within and beyond the ice line can be understood by examining the Stokes number of the largest grains $\mathrm{St}_{\rm max}$ present in each region of the disk (bottom panel of Figure 7). Within $\sim$1 au, $\mathrm{St}_{\rm max}$ can fall down to $\sim 10^{-4}$; these particles will be vertically well-mixed with the gas—i.e. the scale height of dust grains is comparable to that of the gas—flattening the vertical gradient in dust-to-gas ratio. However, outside the ice line, large grains with $\mathrm{St}_{\rm max} \gtrsim 10^{-2}$ are present. These grains are concentrated near the midplane and constitute most of the dust mass budget, resulting in a steep vertical gradient in ϵ. Figure 8 shows the Rosseland mean opacity of the disk as a function of height from the midplane and distance from the star. As expected, we find that the disk opacity is essentially independent of z within the ice line. In contrast, the concentration of large grains near the midplane beyond the ice line leads to a decline in disk opacity as a function of z.

We mark the Hill radius $R_{\rm Hill} = a(M_{\rm p}/3M_*)^{1/3}$ and Bondi radius $R_{\rm Bondi} = GM_{\rm p}/c_s^2$ of a 15 $M_\oplus$ core with a dashed and dotted line respectively in Figures 7 and 8. We choose a mass of 15 $M_\oplus$ as our fiducial case as it is representative of a giant planet core. Planetary cores close to thermal or superthermal mass (equivalently, $R_{\rm Hill} \leq R_{\rm Bondi}$) are expected to accrete gas from heights on the order of the Hill radius (e.g. Lambrechts & Lega 2017). For subthermal cores (equivalently, $R_{\rm Hill} > R_{\rm Bondi}$), on the other hand, the natural length scale is expected to be the Bondi radius (see, e.g., subthermal cases of Ormel et al. 2015 and Fung et al. 2019). The exact origin height of the accretion flow is unclear given how unsteady the flow morphology is in three-dimensional calculations. In this work, we assume that the material accreted by the planet is well represented by the properties of dust and gas present at min($R_{\rm Hill}, R_{\rm Bondi}$) above the disk midplane. In § 4.1, we show the effect of varying this height on the calculated gas-to-core mass fraction of a planet.

Figure 9 highlights how the radial profile of dust-to-gas ratio and dust opacity differ for different heights above the disk

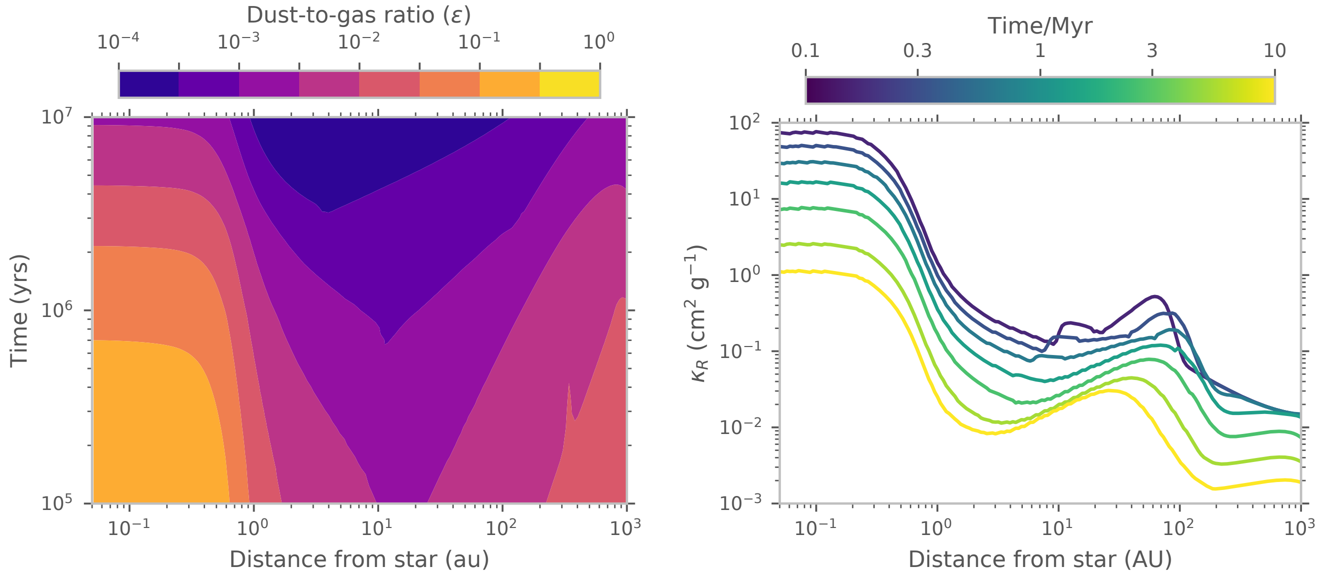

Figure 10. Time evolution of the vertically integrated dust-to-gas ratio ϵ and the Rosseland mean opacity per gram of protoplanetary disk material as a function of distance from the star. Although the absolute values of ϵ and κ_R decline over time due to global accretion of dust onto the star, there is little change in their observed profile shapes as a function of time. The minima in ϵ and κ_R profiles move slightly inward with time as a larger fraction of the outer disk becomes drift dominated.

midplane: $z = 0$ (disk midplane), $z = H_{\rm gas}$, and $z = R_{\rm Hill}$ and $z = \min(R_{\rm Hill}, R_{\rm Bondi})$ for a 15 $M_\oplus$ core. We also provide a calculation of the vertically integrated disk model for comparison. In the top panel we plot κ_R per gram of dust, which depends only on the local size distribution of the dust. The features present in the κ_R profiles result from changes in the relative abundances of the grain sizes that contribute most to the opacity at the local temperature. In the disk midplane beyond the ice line, most of the opacity contribution comes from grains that are $10-100\,\mu$m in size but most of the mass (per gram of dust) resides in grains that are larger than this size range. This leads to a substantial decrease in κ_R per gram of dust in the disk midplane in these regions. Conversely, the high relative abundance of small grains at $z = H_{\rm gas}$ (only small grains can be lifted to this height) leads to a strong enhancement in κ_R per gram of dust at this height. The κ_R profile at $z = R_{\rm Hill}$ and $z = \min(R_{\rm Hill}, R_{\rm Bondi})$ in the top panel of Figure 9 can be understood using these same principles.

Dust-to-gas ratio increases with higher concentration of large grains for a top heavy size distribution and so we observe a flipped behavior for the ϵ ratio profile (middle panel of Figure 9) where it reaches lower values at higher altitudes beyond the ice line. Since larger grains settle close to the midplane, ϵ is highest at the midplane and decreases higher up. The ϵ evaluated at $\min(R_{\rm Hill}, R_{\rm Bondi})$ converges to that of the midplane in the innermost and the outermost region. The former arises from efficient vertical mixing whereas the latter materializes from $R_{\rm Hill}/H_{\rm gas}$ and $R_{\rm Bondi}/H_{\rm gas}$ approaching zero in the outer disk (see $R_{\rm Hill}$ and $R_{\rm Bondi}$ profiles in Figure 7).

In the bottom panel of Figure 9 we plot the mean opacity per gram of protoplanetary disk material, which is the product of the quantities plotted in the upper two panels. Regardless of our vertical location in the disk, we see the same precipitous decline in disk opacity as in the vertically integrated disk model. Notably, κ_R decreases by ~ 2 orders of magnitude between 0.1 au and 5 au at the height of our fiducial planetary core's $R_{\rm Hill}$. Within ~ 10 au, the κ_R profiles for the vertically integrated disk model and the different z values are nearly identical. This happens within the ice line as a result of efficient vertical mixing of grains (i.e. both κ_R per gram of dust and ϵ are roughly constant as a function of z). Beyond the ice line and within 10 au, the sharp decline in ϵ with z is counterbalanced by the increase in κ_R per gram of dust with z to yield a weakly z dependent κ_R (per gram of protoplanetary disk material).

3.5. *Time evolution of the dust opacity*

Up to this point we have presented results from our models after 1 Myr of disk evolution. In this section we explore the time-varying grain size distribution and dust-to-gas-ratio from 0.1 to 10 Myrs, where the lower limit is chosen to represent the plausible time at which massive planetary cores emerge. Figure 10 demonstrates that the absolute values of the dust-to-gas ratio and mean opacity throughout the disk tend to decline over time. This is due to the global depletion of dust in the disk as it gradually accretes onto the star. Because the timescale over which ϵ and κ_R evolve lengthens as time goes on, we present our results as a function of log time. Already by 0.1 Myr, the dust-to-gas ratio and κ_R profiles converge to shapes that are qualitatively similar to those of our fiducial 1 Myr model. Although temporal evolution of the disk after 0.1 Myr leads to $1-2$ orders of magnitude decline in the dust-to-gas ratio and opacity, it has a small effect on their radial gradient in the disk. However, there is a noticeable inward movement of the minima in ϵ and $\kappa_{\rm R}$ profiles with time. This is because as the dust-to-gas ratio declines in the outer disk, the radius at which the disk transitions from being fragmentation-dominated to drift-dominated moves inwards (Equation 16). As we will show in the next section, the overall decline in ϵ and $\kappa_{\rm R}$ over time leads to the enhancement of gas accretion onto planetary cores.

4. IMPLICATIONS FOR PLANET FORMATION

4.1. *Gas accretion mediated by cooling*

Our calculated values for the dust opacity as a function of distance from the star show a dramatic decrease as we move beyond the ice line. We now consider what effect this variation in dust opacity and dust-to-gas ratio might have on the ability of planetary cores to accrete hydrogen-rich envelopes. For cores with masses $\lesssim 20$ $M_\oplus$, the rate of gas accretion onto the planetary core is initially regulated by the envelope's ability to cool and contract (e.g., Lee 2019). This cooling is controlled by the properties of the gas envelope at the innermost radiative-convective boundary (RCB), as most of the cooling luminosity is generated inside the innermost convective zone (Piso & Youdin 2014; Lee et al. 2014).

There is a qualitative difference in the radiative-convective structure of planetary envelopes dominated by dust opacity versus gas opacity. For 'dust-free' envelopes with negligible dust opacity, we expect to see a single convective zone that is connected to the disk via a nearly isothermal radiative zone. However, for 'dusty' envelopes where dust opacity dominates over gas opacity, the evaporation of dust grains deep inside the envelope leads to a dramatic drop in the local envelope opacity, which causes an intermediate radiative zone to form. Lee et al. (2014) show that in this case, the innermost RCB appears at the H_2 dissociation front (~ 2500 K) where H^- opacity starts to dominate.

We expect atmospheres to transition to the 'dust-free' accretion regime when the dust opacity is comparable to the gas opacity at the relevant temperature. In the inner disk (~ 0.1 au), this transition occurs when the dust opacity approaches ~ 0.01 cm^2 g^{-1}. As we move farther out in the disk, the gas opacity decreases sharply ($\lesssim 10^{-4}$ cm^2 g^{-1} at the relevant densities; e.g. Freedman et al. 2014) as the number of available molecular line transitions decreases. In our fiducial disk model for a 15 $M_\oplus$ core, the dust opacity at a height of min($R_{\rm Hill}$, $R_{\rm Bondi}$) above the midplane does not go below the gas opacity limit. Our models therefore predict that accretion at all orbital distance occurs in the 'dusty' regime, whose RCB opacity—which controls the rate of cooling and therefore accretion—is given by the H^- opacity (Lee & Chiang 2015):

$$\kappa(\mathrm{H}^-) \sim 3\times10^{-2}\mathrm{cm}^2\mathrm{g}^{-1}\left(\frac{\rho}{10^{-4}\ \mathrm{g\ cm}^{-3}}\right)^{0.5}\left(\frac{T}{2500\ \mathrm{K}}\right)^{7.5}\left(\frac{Z}{0.02}\right)^{1}. \quad (17)$$

The only influence dust has on the H^- opacity is via the metallicity dependence Z of the gas. We set Z equal to the local dust-to-gas ratio in our gas accretion calculations as the metals delivered via dust are present in the gas phase at the H_2 dissociation front. Equating Z to the dust-to-gas ratio is justified because the Z dependence of $\kappa(H^-)$ results from its dependence on the availability of free electrons, most of which are sourced from metallic species. Although some of these metals might be present in the gas, the dust contribution dominates. This is likely to be true even in the most dust depleted regions of the outer disk as CO is predicted to be the dominant gas phase metal in this region. This molecule does not dissociate until much deeper in the planetary atmosphere, and hence it will not contribute free electrons in the region where H^- opacity becomes important.

We use this information to calculate gas accretion rates onto a planetary core as a function of disk location and time using the analytical scaling laws provided by Lee & Chiang (2015), modified for the linear dependence on the bound radius and the weak dependence on nebular density (see Lee & Connors 2020). The gas-to-core mass ratio (GCR) at time t in the 'dusty' planetary envelope regime is given by:

$$\mathrm{GCR} \sim 0.06\, f_{\rm R}\left(\frac{\Sigma_g}{2000\ \mathrm{g\ cm}^{-3}}\right)^{0.12}\left(\frac{t}{1\ \mathrm{Myr}}\right)^{0.4}\left(\frac{\nabla_{\rm ad}}{0.17}\right)^{3.4}\left(\frac{2500\ \mathrm{K}}{T_{\rm rcb}}\right)^{4.8}\left(\frac{0.02}{Z}\right)^{0.4}\left(\frac{\mu_{\rm rcb}}{2.37}\right)^{3.4}\left(\frac{M_{\rm core}}{5M_\oplus}\right)^{1.7}. \quad (18)$$

Here, $f_{\rm R}$ is the bounded radius of a planet as a fraction of its min($R_{\rm Hill}$, $R_{\rm Bondi}$) and we set it equal to 0.2 (e.g. Fung et al. 2019). The updated scaling law provided by Lee & Connors (2020) also allows us to incorporate the dependence of GCR on the gas surface density Σ_g, which we obtain from our disk model. The normalization factor of 0.06 is valid for $\Sigma_g < 0.1$ MMEN at 0.1 au. $\nabla_{\rm ad}$, $T_{\rm rcb}$ and $\mu_{\rm rcb}$ are the adiabatic gradient, temperature, and the mean molecular weight evaluated at the RCB. We assume a fixed value of $T_{\rm rcb} = 2500$ K and $\nabla_{\rm ad} = 0.17$, appropriate for the innermost RCB at the H_2 dissociation front, for all our calculations. We calculate $\mu_{\rm rcb}$ assuming a $\mu = 2.3$ for a pure hydrogen-helium mixture (solar abundance ratio) and $\mu = 17$ for a pure metal-rich atmosphere. For the most metal-rich gases ($Z \gtrsim 0.2$; Lee & Chiang 2016), the strong dependence of GCR on $\mu_{\rm rcb}$ dominates

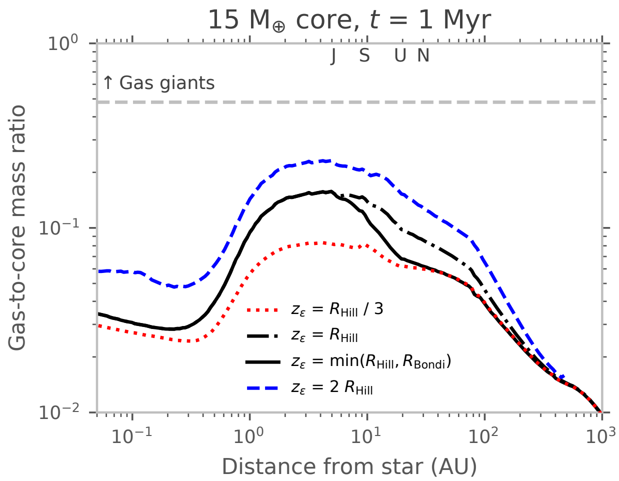

Figure 11. The gas-to-core mass ratio (GCR) at t = 1 Myr for a 15 $M_\oplus$ core as a function of distance from the star, assuming the core starts accreting at 0.1 Myr. Here, we vary the height z_ϵ from which gas is accreted by the planet. A GCR of 0.48 is marked with a dashed grey line, indicating the threshold for the onset of runaway gas accretion (Lee et al. 2014).

over the metallicity-dependent increase in opacity, allowing for rapid accretion (Venturini et al. 2015). Our models predict that the dust-to-gas ratio throughout the disk will remain below this critical value for a majority of the disk lifetime. $Z > 0.2$ in the inner disk only at very early stages (< 0.1 Myr) when core formation is still likely ongoing.[4] For the entirety of the duration of gas accretion that we model (0.1–10 Myrs), an increased Z therefore acts to reduce the accretion rate by increasing the gas opacity at the RCB. We incorporate the time dependence of Σ_g, Z, and $\mu_{\rm rcb}$ in our calculation of GCR by numerically differentiating Equation 18 with respect to time and integrating between $t_0 = 0.1$ Myr (the emergence of the core) and time t (in the range $1-10$ Myr) at which the planet stops accreting.

Figure 11 shows the gas-to-core mass ratio (GCR) calculated for our fiducial core mass of 15 $M_\oplus$ as a function of distance from the star at t = 1 Myr. We vary the height z_ϵ from which material is accreted by the planet, which affects the metallicity (dust-to-gas ratio) of the accreted material and therefore the GCR profile. Along with our default value of $z_\epsilon = \min(R_{\rm Hill}, R_{\rm Bondi})$, we also show GCR profiles for $z_\epsilon = [1/3, 1, 2] \times R_{\rm Hill}$. Inside ~ 1 au, the relatively high Z (~ 0.1) produces a GCR in the range $0.03-0.06$ for a wide range of z_ϵ. However, the sharp drop in Z beyond ~ 1 au (see middle panel of Figure 9) leads to a rise in the amount of gas accreted by the planetary core, reaching a peak value of ~ 0.15 in the $1-10$ au region of the disk for $z_\epsilon = \min(R_{\rm Hill}, R_{\rm Bondi})$. Beyond ~ 10 au, the metallicity of the gas (i.e. dust-to-gas ratio) at $R_{\rm Hill}$ and $R_{\rm Bondi}$ rises again as the Hill and Bondi radii shrink relative to the disk scale height, which leads to a decline in GCR. The weak dependence of GCR on Σ_g also contributes to a decline in GCR with distance. We note that the peak GCR value in the intermediate $1-10$ au region increases with the height above the midplane from which the planet accretes as the dust-to-gas ratio is a strongly decreasing function of z in this region. Overall, Figure 11 demonstrates that the amount of gas accreted by a planetary core during the accretion-by-cooling phase, and hence its ability to reach the threshold for runaway growth, varies significantly as a function of its location in the disk.

4.2. *Consequences for giant planet formation and demographics*

Our calculations provide a natural explanation for the observed peak in the gas giant planet occurrence rate at ∼1–10 au as measured by radial velocity and direct imaging surveys (e.g. Baron et al. 2019; Fernandes et al. 2019; Fulton et al. 2019; Nielsen et al. 2019; Wittenmyer et al. 2020). Figure 12 demonstrates that the location of the most favorable sites for rapid gas accretion is driven by the decrease in dust-to-gas ratio just beyond the ice line where relatively larger grains undergo efficient radial drift and vertical settling. We note that the nucleation of gas giants requires relatively massive cores ($\sim 15 M_\oplus$) that assemble early (i.e., accrete gas for at least 3–10 Myrs). Lighter cores and/or those that assemble late (i.e., accrete gas for shorter amount of time) necessarily grow into planets with less massive envelopes. Although it is difficult to obtain good observational constraints on the core masses of extrasolar Jupiters (Thorngren & Fortney 2019), we note that the cores of sub-Saturns—planets that were on the verge of runaway but were halted in growth before they became gas giants—are better-constrained and appear to range between ~ 15–$20 M_\oplus$ in the limiting case where all metals are assumed to be sequestered in the core (Petigura et al. 2017; Lopez & Fortney 2014).

The same change in fragmentation velocity of grains across the ice line that we invoke in our model may also result in the formation of more massive cores outside the ice line (e.g. Morbidelli et al. 2015; Venturini et al. 2020), reinforcing our results that gas giants are more likely to originate farther away from the star. Our work further demonstrates that the dust-to-gas ratio is expected to be radially-variant and that it reaches a local minimum at a specific range of orbital distances (1–10 au), creating a preferred zone of rapid gas accretion. Qualitatively, our solar system also fits into

[4] We note that late-stage pollution of an envelope by ambient solids could enhance the interior metallicity beyond $Z \sim 0.2$ and trigger rapid gas accretion (Hori & Ikoma 2011). The short dynamical timescale in the inner disk suggests that the solids there most likely lock into planetary cores before the late-stage disk gas dispersal, and so such late-stage pollution is more likely to occur in the outer disk.

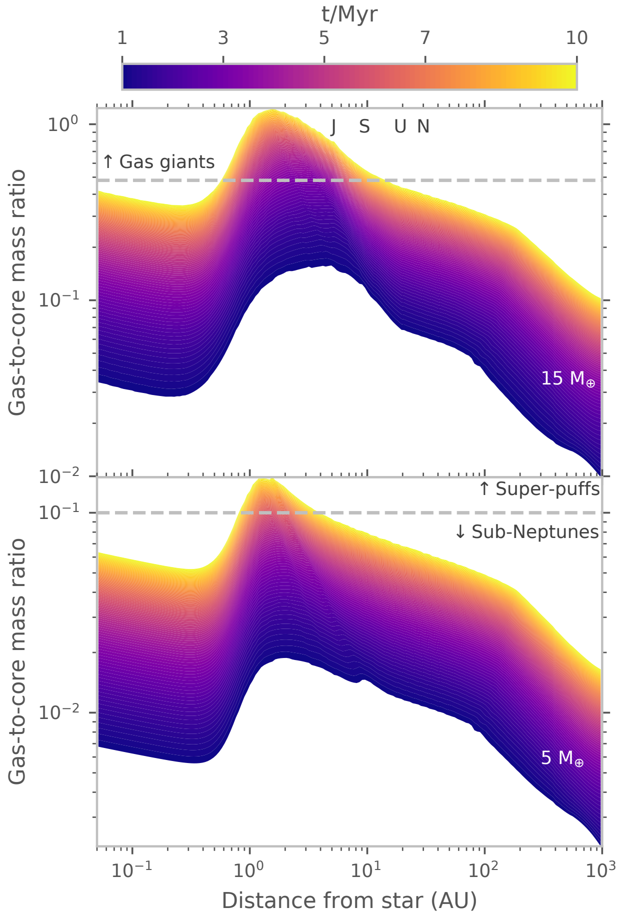

Figure 12. The gas-to-core mass ratio (GCR) as a function of distance from the star for 5 $M_\oplus$ (bottom panel) and 15 $M_\oplus$ (top panel) cores for time t in the range $1-10$ Myr, assuming they start accreting material present at min($R_{\rm Hill}$, $R_{\rm Bondi}$) at 0.1 Myr. GCR of 0.48 (onset of runaway gas accretion Lee et al. 2014) and GCR = 0.1 (for sub-Neptunes and super-puffs) are marked with dashed grey lines in the top and bottom panels respectively. The locations of solar system giant planets are marked along the abscissa at the top.

our picture, with gas giants Jupiter and Saturn forming at intermediate distances where the GCR peaks and Uranus and Neptune forming further out where the GCR declines with distance (Morbidelli et al. 2007; Batygin & Brown 2010).

4.3. *Formation of sub-Neptunes and super-puffs*

Close-in sub-Neptunes appear to possess primordial hydrogen-rich envelopes that are a few percent of the total planet mass (e.g., Lopez & Fortney 2014; Wolfgang & Lopez 2015; Ning et al. 2018). Given their estimated core masses of $4-8$ $M_\oplus$ (Wu 2019; Rogers & Owen 2020), it is difficult to explain why these planets did not undergo runaway gas accretion and turn into gas giants assuming they formed in MMEN and accreted solar metallicity gas. Previous studies have proposed three potential solutions: 1) accretion of metal rich gas, which increases the envelope opacity and slows the gas accretion rate during the cooling growth phase (e.g. Lee et al. 2014; Chen et al. 2020), 2) late-time core assembly, so that there is a very short period for the planet to accrete prior to the dispersal of the gas disk (Lee & Chiang 2016), and 3) a flow of high entropy gas into the Hill sphere of the growing planet that prevents it from cooling (Ormel et al. 2015; Béthune & Rafikov 2019, but see Kurokawa & Tanigawa 2018). Scenario 1 in and of itself applies for either dusty or dust-free accretion but it is more effective for dusty accretion as its overall higher opacity delays accretion even more. Our work revisits the first scenario in the context of in situ, dusty gas accretion.

Our results suggest that the enhanced dust to gas ratio in the inner disk is sufficient to limit the envelope masses/accretion rates of sub-Neptunes forming in this region. We find that for a representative 5 $M_\oplus$ core, the enhanced dust-to-gas ratio inside the ice line is just enough to prevent the accretion of a massive gas envelope (Figure 12, bottom panel). If the metallicity is too high ($Z > 0.2$), the enhancement in the mean molecular weight of the gas can expedite gas accretion (Lee & Chiang 2015; Venturini et al. 2015). For our fiducial choice of fragmentation velocities and turbulence parameter (as well as for a large swath of the parameter space), Z stays below 0.2 in the inner disk after 0.1 Myrs. As shown in Figure 12, a $5M_\oplus$ core inside 1 au attains a few percent by mass envelope, consistent with the measured masses and radii of sub-Neptunes, even if the core assembled early and accreted gas for the full 10 Myrs. We note that this result is not mutually exclusive with late-time core assembly for sub-Neptunes. The late-time, gas-poor environment favors the build-up of $\sim 5M_\oplus$ sub-Neptune cores by a series of collisional mergers. Such mergers are necessary as the isolation masses, either from planetesimal (see Dawson & Johnson 2018, their Figure 2) or pebble accretion (see, e.g., Bitsch et al. 2018; Fung & Lee 2018) are on the order an Earth mass or smaller in the inner disk. Furthermore, late-time assembly of sub-Neptunes prevents inward migration of these planets once they assemble (Lee & Chiang 2016).

Our models also provide support for previously published hypotheses about the origin of 'super-puffs', a rare class of planets with giant planet like radii (4–8 $R_\oplus$) and super-Earth like masses (2–5 $M_\oplus$) (Lee & Chiang 2016). The low bulk densities of these planets imply that they possess hydrogen-rich envelopes that are tens of % by mass (Masuda 2014; Jontof-Hutter et al. 2014; Ofir et al. 2014). Although the gas mass fraction of some super-puffs may be overestimated due to the inflation of planetary radii measurements by photochemical hazes lofted by outflowing gas, the majority of super-puffs do appear to have accreted substantially more gas than sub-Neptunes (Wang & Dai 2019; Libby-Roberts et al.

2020; Gao & Zhang 2020; Chachan et al. 2020). It is difficult to explain how these planets, which have core masses similar to those of sub-Neptunes, could have accreted an order of magnitude more gas in their present-day locations (Ikoma & Hori 2012; Lee & Chiang 2016). Lee & Chiang (2016) proposed that super-puffs might form by accreting 'dust-free' gas (dust opacity lower than gas opacity) beyond ~ 1 au. Although the dust opacity in our models is never low enough to qualify as dust-free, we find that the decrease in opacity beyond the ice line does indeed lead to significantly higher gas accretion rates and GCRs (Figure 12). All of the currently known super-puffs are in or near orbital resonances with other planets[5], which requires relatively smooth convergent migration (e.g. Cresswell & Nelson 2006). This is consistent with a scenario in which super-puffs formed beyond ~ 1 au and then migrated inward via interactions with the protoplanetary gas disk. As Figure 12 shows, the creation of super-puffs require their cores to have assembled early so that the total gas accretion time is longer. The requirement for early stage core assembly is also in agreement with the migratory origin of super-puffs as disk-induced migration requires a gas-rich environment.

5. DISCUSSION AND CONCLUSIONS

In this work we use dust evolution models to demonstrate that the dust opacity and dust-to-gas ratio in protoplanetary disks is expected to be radially and vertically variant, with significant implications on planet formation. This is a result of grain growth and transport, which produce a highly non-uniform dust-to-gas ratio in the disk and generate top heavy size distributions with grains that are orders of magnitude larger than the maximum grain size in the commonly-assumed ISM distribution. We explore the sensitivity of our models to assumptions about the disk turbulence and fragmentation velocities and find that we obtain qualitatively similar results over a wide range of plausible values.

Models with a substantial difference in $v_{\rm frag}$ across the ice line and moderate-to-low turbulence values $\alpha_{\rm t} \lesssim 10^{-3}$ produce the largest radial variations in dust opacity. A large change in $v_{\rm frag}$ across the ice line leads to a large difference in the Stokes number St of the largest grains within and beyond the ice line. In the inner disk with smaller St (well-coupled to gas), dust grains pile up radially and mix well vertically. In the outer disk with larger St (more decoupled from gas), dust grains drift in rapidly and settle to the midplane. As a result, the inner disk is characterized by high dust-to-gas ratio that is near constant with height, whereas the outer disk is characterized by lower dust-to-gas ratio that decreases even further away from the midplane.

We use our location-dependent dust-to-gas ratio and dust opacity to calculate gas accretion rates onto planetary cores as a function of distance from the star. If we assume that the growing planet predominately accretes material present at min($R_{\rm Hill}$, $R_{\rm Bondi}$) above the midplane, we find that the gas-to-core mass ratio (GCR) is a strong function of its location in the disk. Within the ice line, gas accretion onto the core is suppressed by the high dust-to-gas ratio. At intermediate distance beyond the ice line ($1-10$ au in our fiducial model), there is a steep decline in the dust-to-gas ratio, causing the GCR to rise and making it easier for cores to reach the threshold for runaway gas accretion. Beyond this point the dust-to-gas ratio increases again as the growing planet accretes from a region closer to the disk midplane (min($R_{\rm Hill}$, $R_{\rm Bondi}$) / $H_{\rm gas}$ declines with distance). We conclude that dust-gas dynamics favor gas giant planet formation at intermediate distances, potentially explaining the peak in the giant planet occurrence rate vs. orbital distance (Fulton et al. 2019). Our results also provide support for the hypothesis that super-puffs likely formed beyond the ice line, as the lower dust-to-gas ratio in this region can substantially accelerate their gas accretion rates.

We note that the same models presented in this study could be used to constrain the core mass distribution of gas giant exoplanets by quantifying the fraction of planets that undergo runaway gas accretion as a function of location (e.g. Lee 2019). Previous studies on core formation have argued that a change in $v_{\rm frag}$ across the ice line could lead to a significant increase in core masses outside the ice line (Morbidelli et al. 2015; Venturini et al. 2020). In a future study we will explore whether the radially-varying dust opacity alone is sufficient to reproduce the observed mass-period distribution of gas giant exoplanets, or whether it is also necessary to invoke a radially varying core mass function or large scale migration. These same models could also be used to explore why outer gas giants are commonly accompanied by inner super-Earths (Zhu & Wu 2018; Bryan et al. 2019).

In this study we have limited ourselves to a single fiducial disk model to show how dust opacity varies with radial distance. However, observations of protoplanetary disks indicate that there is a large variation in disk properties such as the disk mass, size, lifetime, and metallicity as well as the mass and luminosity of protostars (Andrews et al. 2018; Long et al. 2018; Long et al. 2019). In future studies, we will investigate how dust evolution and gas accretion onto planetary cores depend on these properties and whether the diversity of exoplanets is thus linked to the diversity in disk and stellar properties. Potential improvements for these calculations include accounting for the conversion of dust to planetesimals/planetary cores on the dust mass budget and the

[5] Most super-puffs orbit dim stars, which makes it hard to measure their masses with the radial velocity technique. Their masses have typically been determined by transit timing variations, which by definition require them to be in dynamically interacting multi-planet systems.

effect of planet-disk interaction on dust growth and dynamics. In particular, as planetary cores become massive enough to perturb the gas disk, pressure maxima outside the planet's orbit traps some of the dust. This could affect the local size distribution and radial migration of dust as well as the dust-to-gas ratio of the material accreted by the growing planet (Chen et al. 2020). We expect these effects to be perturbative and more localized in nature and the global dust evolution to broadly follow the picture we have painted in this work. Overall, the radial variation of dust-to-gas ratio and dust opacity have a substantial effect on the ability of planetary cores to accrete gas and should be considered in models of planet formation.

ACKNOWLEDGEMENTS

We are indebted to Dave Stevenson and Yanqin Wu for giving us feedback on this manuscript. Y.C. is grateful to Til Birnstiel for providing excellent public repositories that this work relies on. Support for this work was provided by NASA through Space Telescope Science Institute grants GO-14682 and GO-15138.

REFERENCES

Alexander, D. R., & Ferguson, J. W. 1994a, International Astronomical Union Colloquium, 146, 149
—. 1994b, ApJ, 437, 879
Andrews, S. M. 2015, PASP, 127, 961
Andrews, S. M., Huang, J., Pérez, L. M., et al. 2018, ApJL, 869, L41
Banzatti, A., Pinilla, P., Ricci, L., et al. 2015, ApJL, 815, L15
Baron, F., Lafrenière, D., Artigau, É., et al. 2019, AJ, 158, 187
Batalha, N. M., Rowe, J. F., Bryson, S. T., et al. 2013, ApJS, 204, 24
Batygin, K., & Brown, M. E. 2010, ApJ, 716, 1323
Bell, K. R., & Lin, D. N. C. 1994, Apj, 427, 987
Béthune, W., & Rafikov, R. R. 2019, MNRAS, 488, 2365
Birnstiel, T., Andrews, S. M., Pinilla, P., & Kama, M. 2015, ApJL, 813, L14
Birnstiel, T., Dullemond, C. P., & Brauer, F. 2010, A&A, 513, A79
Birnstiel, T., Klahr, H., & Ercolano, B. 2012, A&A, 539, A148
Birnstiel, T., Ormel, C. W., & Dullemond, C. P. 2011, A&A, 525, 1
Birnstiel, T., Dullemond, C. P., Zhu, Z., et al. 2018, ApJ, 869, L45
Bitsch, B., Johansen, A., Lambrechts, M., & Morbidelli, A. 2015, A&A, 575, 28
Bitsch, B., Morbidelli, A., Johansen, A., et al. 2018, A&A, 612, A30
Blum, J., & Wurm, G. 2008, ARA&A, 46, 21
Bowler, B. P., & Nielsen, E. L. 2018, Occurrence Rates from Direct Imaging Surveys, ed. H. J. Deeg & J. A. Belmonte, 155
Brauer, F., Dullemond, P., & Henning, T. 2008, A&A, 480, 859
Bryan, M. L., Knutson, H. A., Lee, E. J., et al. 2019, AJ, 157, 52
Carrera, D., Gorti, U., Johansen, A., & Davies, M. B. 2017, ApJ, 839, 16
Chachan, Y., Jontof-Hutter, D., Knutson, H. A., et al. 2020, AJ, 160, 201
Chen, Y.-X., Li, Y.-P., Li, H., & Lin, D. N. C. 2020, ApJ, 896, 135
Chiang, E., & Youdin, A. 2010, AREPS, 38, 493
Chiang, E. I., & Goldreich, P. 1997, ApJ, 490, 368
Cieza, L. A., Casassus, S., Tobin, J., et al. 2016, Nature, 535, 258
Cimerman, N. P., Kuiper, R., & Ormel, C. W. 2017, MNRAS, 471, 4662
Cresswell, P., & Nelson, R. P. 2006, A&A, 450, 833
Cumming, A., Butler, R. P., Marcy, G. W., et al. 2008, PASP, 120, 531
D'Alessio, P., Calvet, N., & Hartmann, L. 2001, ApJ, 553, 321
D'Alessio, P., Canto, J., Calvet, N., & Lizano, S. 1998, ApJ, 500, 411
Dawson, R. I., & Johnson, J. A. 2018, ARA&A, 56, 175
Draine, B. T. 2003, ApJ, 598, 1026
—. 2006, ApJ, 636, 1114
Draine, B. T., & Lee, H. M. 1984, ApJ, 285, 89
Drążkowska, J., & Alibert, Y. 2017, A&A, 608, 92
Dressing, C. D., & Charbonneau, D. 2015, ApJ, 807, 45
Fernandes, R. B., Mulders, G. D., Pascucci, I., Mordasini, C., & Emsenhuber, A. 2019, ApJ, 874, 81
Flaherty, K. M., Hughes, A. M., Rosenfeld, K. A., et al. 2015, ApJ, 813, 99
Flaherty, K. M., Hughes, A. M., Teague, R., et al. 2018, ApJ, 856, 117
Flaherty, K. M., Hughes, A. M., Rose, S. C., et al. 2017, ApJ, 843, 150
Freedman, R. S., Lustig-Yaeger, J., Fortney, J. J., et al. 2014, ApJSS, 214
Fressin, F., Torres, G., Charbonneau, D., et al. 2013, ApJ, 766, 81
Fromang, S., & Nelson, R. P. 2009, A&A, 496, 597
Fulton, B., Rosenthal, L., Howard, A., Hirsch, L., & Isaacson, H. 2019, in Extreme Solar Systems 4, Bulletin of the American Astronomical Society, Vol. 51, No. 6, Vol. 51, 401.01
Fung, J., Artymowicz, P., & Wu, Y. 2015, ApJ, 811, 101
Fung, J., & Lee, E. J. 2018, ApJ, 859, 126
Fung, J., Zhu, Z., & Chiang, E. 2019, ApJ, 887, 152
Gao, P., & Zhang, X. 2020, ApJ, 890, 93
Gundlach, B., & Blum, J. 2015, ApJ, 798
Gundlach, B., Schmidt, K. P., Kreuzig, C., et al. 2018, MNRAS, 479, 1273

Hayashi, C. 1981, Progress of Theoretical Physics Supplement, 70, 35
Henning, T., & Stognienko, R. 1996, A&A, 311, 303
Hori, Y., & Ikoma, M. 2011, MNRAS, 416, 1419
Howard, A. W., Marcy, G. W., Bryson, S. T., et al. 2012, ApJSS, 201, 15
Ikoma, M., & Hori, Y. 2012, ApJ, 753, 66
Ikoma, M., Nakazawa, K., & Emori, H. 2000, ApJ, 537, 1013
Jontof-Hutter, D., Lissauer, J. J., Rowe, J. F., & Fabrycky, D. C. 2014, ApJ, 785, 15
Kimura, H., Wada, K., Kobayashi, H., et al. 2020, MNRAS, 1813, 1801
Kitzmann, D., & Heng, K. 2018, MNRAS, 475, 94
Kurokawa, H., & Tanigawa, T. 2018, MNRAS, 479, 635
Lambrechts, M., & Lega, E. 2017, A&A, 606, A146
Laor, A., & Draine, B. T. 1993, ApJ, 402, 441
Lee, E. J. 2019, ApJ, 878, 36
Lee, E. J., & Chiang, E. 2015, ApJ, 811, 41
—. 2016, ApJ, 817, 90
Lee, E. J., Chiang, E., & Ormel, C. W. 2014, ApJ, 797, 95
Lee, E. J., & Connors, N. J. 2020, arXiv e-prints, arXiv:2008.01105
Libby-Roberts, J. E., Berta-Thompson, Z. K., Désert, J.-M., et al. 2020, AJ, 159, 57
Long, F., Pinilla, P., Herczeg, G. J., et al. 2018, ApJ, 869, 17
Long, F., Herczeg, G. J., Harsono, D., et al. 2019, ApJ, 882, 49
Lopez, E. D., & Fortney, J. J. 2014, ApJ, 792, 1
Lynden-Bell, D., & Pringle, J. E. 1974, MNRAS, 168, 603
Masuda, K. 2014, ApJ, 783, 53
Mathis, J. S., Rumpl, W., & Nordsieck, K. H. 1977, ApJ, 217, 425
Miyake, K., & Nakagawa, Y. 1993, Icarus, 106, 20
Morbidelli, A., Lambrechts, M., Jacobson, S., & Bitsch, B. 2015, Icarus, 258, 418
Morbidelli, A., Tsiganis, K., Crida, A., Levison, H. F., & Gomes, R. 2007, AJ, 134, 1790
Mordasini, C. 2018, in Handbook of Exoplanets (Cham: Springer International Publishing), 2425–2474
Morton, T. D., & Swift, J. 2014, ApJ, 791, 10
Mulders, G. D., & Dominik, C. 2012, A&A, 539, 9
Musiolik, G., & Wurm, G. 2019, ApJ, 873, 58
Nielsen, E. L., De Rosa, R. J., Macintosh, B., et al. 2019, AJ, 158, 13
Ning, B., Wolfgang, A., & Ghosh, S. 2018, ApJ, 869, 5
Oberg, K. I., & Bergin, E. A. 2020, Physics Reports (in press)
Oberg, K. I., Murray-Clay, R., Bergin, E. A., et al. 2011, ApJL, 743, L16
Ofir, A., Dreizler, S., Zechmeister, M., & Husser, T.-O. 2014, A&A, 561, A103
Ormel, C. W., & Cuzzi, J. N. 2007, A&A, 466, 413
Ormel, C. W., Shi, J.-M., & Kuiper, R. 2015, MNRAS, 447, 3512
Petigura, E. A., Sinukoff, E., Lopez, E. D., et al. 2017, AJ, 153, 142
Petigura, E. A., Marcy, G. W., Winn, J. N., et al. 2018, AJ, 155, 89
Pinilla, P., Klarmann, L., Birnstiel, T., et al. 2016, A&A, 585, A35
Pinilla, P., Pohl, A., Stammler, S. M., et al. 2017, ApJ, 845, 68
Pinte, C., Dent, W. R. F., Menard, F., et al. 2016, ApJ, 816, 25
Piso, A. M. A., & Youdin, A. N. 2014, ApJ, 786, 21
Piso, A.-M. A., Youdin, A. N., Murray-Clay, R. A., et al. 2015, ApJ, 800, 82
Pollack, J. B., Hubickyj, O., Bodenheimer, P. H., et al. 1996, Icarus, 124, 62
Poppe, T., Blum, J., & Henning, T. 2000, ApJ, 533, 454
Rogers, J. G., & Owen, J. E. 2020, arxiv:2007.11006
Savvidou, S., Bitsch, B., & Lambrechts, M. 2020, A&A, 640, 63
Shakura, N. I., & Sunyaev, R. A. 1973, A&A, 24, 337
Steinpilz, T., Teiser, J., & Wurm, G. 2019, ApJ, 874, 60
Stevenson, D. J. 1982, Planet. Space Sci, 30, 755
Testi, L., Natta, A., Shepherd, D. S., & Wilner, D. J. 2003, A&A, 403, 323
Thorngren, D., & Fortney, J. J. 2019, ApJ, 874, L31
Turner, N. J., Fromang, S., Gammie, C., et al. 2014, in Protostars and Planets VI (University of Arizona Press), 411
van de Hulst, H. C. 1957, Light Scattering by Small Particles (John Wiley & Sons)
Venturini, J., Alibert, Y., Benz, W., & Ikoma, M. 2015, A&A, 576, A114
Venturini, J., Guilera, O. M., Ronco, M. P., & Mordasini, C. 2020, A&A
Wada, K., Tanaka, H., Okuzumi, S., et al. 2013, A&A, 559, A62
Wang, L., & Dai, F. 2019, ApJ, 873, L1
Warren, S. G., & Brandt, R. E. 2008, JGRA, 113
Weidenschilling, S. 1977, MNRAS, 57
Wittenmyer, R. A., Butler, R. P., Tinney, C. G., et al. 2016, ApJ, 819, 28
Wittenmyer, R. A., Wang, S., Horner, J., et al. 2020, MNRAS, 492, 377
Wolfgang, A., & Lopez, E. 2015, ApJ, 806, 183
Wu, Y. 2019, ApJ, 874, 91
Zhang, M., Chachan, Y., Kempton, E. M.-R., & Knutson, H. A. 2019, PASP, 131, 034501
Zhang, M., Chachan, Y., Kempton, E. M.-R., Knutson, H. A., & Chang, W. H. 2020, ApJ, 899, 27
Zhu, W., & Wu, Y. 2018, AJ, 156, 92